Quantum multilateration: Subdiffraction emitter pair localization via three spatially separate Hanbury Brown and Twiss measurements

Josef G. Worboys [*], Daniel W. Drumm [†], and Andrew D. Greentree [‡]
Australian Research Council Centre of Excellence For Nanoscale Biophotonics, RMIT University, Melbourne 3001, Australia

Typically, optical microscopy uses the wavelike properties of light to image a scene. However, photon arrival times provide more information about emitter properties than the classical intensity alone. Here we show that the Hanbury Brown and Twiss experiment (second-order correlation function) measures the relative brightness of two single-photon emitters. By combining the total number of detected photons with the zero-lag value of the correlation function, the positions and relative brightness of two emitters in two dimensions can be resolved from only three measurement positions: trilateration. This result is impossible to achieve on the basis of classical intensity measurements alone and represents a minimal demonstration of the advantage gained using quantum measurements over conventional classical microscopy. The effective point-spread function for imaging scales approximately as the inverse square root of the acquisition time.

I. INTRODUCTION

Optical microscopy is one of the most important tools for the understanding of biology. Conventional microscopy is limited by the wavelike nature of light, and the associated diffraction limit which imposes a fundamental restriction on imaging resolution in the absence of *a priori* information of the system being imaged. There are now many techniques to beat the diffraction limit, defining the emerging field of optical nanoscopy. Such techniques either use nonlinear optical processes, blinking, *ansätzer* about the system, or quantum techniques to derive subwavelength information. Interestingly, all of the standard super-resolution techniques [1–3] appear to have a qualitatively similar scaling law of resolution with probe intensity ($1/\sqrt{N}$), suggesting that a common framework exists for understanding the fundamental limits of resolution in microscopy [4,5]. Heisenberg resolution scaling ($1/N$) is possible in certain circumstances [6,7]. However, such scaling requires indistinguishable photons and (usually) nontrivial quantum entanglement, which makes those protocols unsuitable for conventional confocal microscopy, as discussed here.

Quantum correlations are an intriguing resource for optical nanoscopy. The Hanbury Brown and Twiss (HBT) experiment was initially developed as a method of determining stellar parallax [8] and was the first experiment to definitively prove the quantization of the electromagnetic field. In its simplest form, HBT uses two single-photon detectors that receive signals from the same optical point-spread function (PSF). When an emitter produces no more than one photon at any given time, quantization of the field means that the photon cannot be detected at both detectors simultaneously, and therefore the cross-correlated signal must go to zero at zero time delay.

Quantum correlation microscopy (QCM) uses measurements derived from HBT signals across multiple emitters to improve microscopy resolution [9]. This scheme was first introduced in a confocal setup by Hell *et al.* [10], experimentally demonstrated to higher orders in wide-field imaging by Schwarz and Oron [11], and with confocal microscopy by Monticone *et al.* [12]. By considering higher-order correlation functions of the field, the effective point-spread function is raised to the power of the order of the correlation. This leads to a reduction in the width of the point-spread function [10,13]. Alternatively, we may view the correlation function as providing information about the number of emitters, which can be used in centroid-type fitting algorithms [14–16], and this is the approach taken here. In both approaches, using quantum correlations of the field provides an improvement in confocal and wide-field resolution that scales as $\sqrt{k}$, where k is the order of the quantum correlation. Related, but distinct methods of super-resolution imaging using correlated photon detection at different locations have been studied for enhancing spatial resolution for thermal sources, including pointlike and extended sources, and spatial mode demultiplexing [17–21]. A review covering quantum measurement approaches applied to imaging can be found in Ref. [22].

Trilateration is the determination of the position of an object in two dimensions on the basis of the intersection of three structures with circular or spherical symmetry and finds practical application in fields such as surveying and satellite global positioning systems [23,24]. The task of locating a single-photon emitter or emitters on a two-dimensional plane using confocal microscopy [25–27] can also be described as a problem in (multi)lateration [28], although it is usually not investigated as such.[1] For brevity, we consider the PSF to represent the product of the

---

[*]josefgworboys@gmail.com; josef.worboys@rmit.edu.au
[†]dr.daniel.drumm@gmail.com
[‡]andrew.greentree@rmit.edu.au

---

[1]Confocal microscopy is not inherently lateration as it does not rely on photon times of arrival (PTOA), which in the context of lateration

illumination and collection point-spread functions. Understanding the minimum requirements on the number of measurement locations (PSFs) is important as conventional scanning confocal techniques are known to be suboptimal for search [29].

Here we show that quantum measurements from three locations suffice to determine the location of two particles separated by less than the Rayleigh limit, in two dimensions in the plane perpendicular to the optical axis. Such a determination on the basis of intensity-only measurements is impossible as there are five unknown quantities (the x and y locations of each emitter and their relative brightness) and only three measurement results. Our result constitutes a minimal demonstration of the advantage that QCM provides over conventional microscopy, and represents an example demonstration that is impossible for classical (intensity-only) imaging. We construct explicit simulations of the HBT cross-correlation function for the case of two emitters of unequal brightness and show their predicted origins relative to simple measurements of the intensity. We focus on the ideal case here; however, this work is specifically useful in studying problems such as dimerization, which is important in certain biochemical reactions [30–33]. We also explore the effects of increasing the number of measurement locations, comparing the efficiency of the quantum schemes with intensity-based imaging.

This paper is organized as follows. We begin by describing the expected HBT signals for varying source conditions, highlighting the cross-correlation function as a measure of the emitter brightness asymmetry and of background emission. We then show trilateration/multilateration for two emitters, including the predicted resolution as a function of measurement time. Finally, we show the expected scalings for the protocol, including results for up to 24 measurement locations.

II. PROPERTIES OF THE HANBURY BROWN AND TWISS EXPERIMENT FOR TWO OR MORE PARTICLES

The HBT experiment measures photon-detection coincidences between two detectors (D_1, D_2) monitoring the same spatial region as a function of time. This experiment is depicted schematically in Fig. 1(a), where the excitation light source has not been shown, but would usually be applied confocally. Analytically obtained HBT results are shown in Fig. 1(b) for the case of two emitters of unequal brightness, and a single emitter.

The coincidence rate is expressed as a function $g^{(2)}$ of the time delay τ between photon detections at the different detectors, where the number of coincidences detected at τ is normalized by the uncorrelated coincidences at $\tau = \pm\infty$. The uncorrelated coincidences are in turn a measure of the total number of single-photon clicks, i.e., the intensity I. Here,

———

is usually used to measure the distance from the source to object to detector. Instead, confocal microscopy aggregates signals for each image pixel. Although PTOA is not usually available in microscopy, the variation in brightness of the emitter within a circularly symmetric PSF acts as a proxy for distance determination.
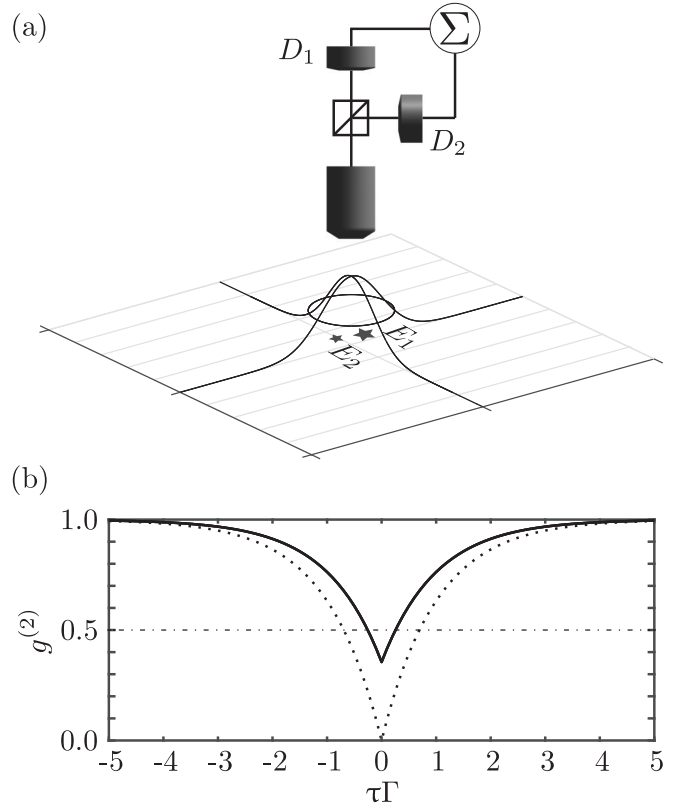

FIG. 1. (a) Schematic of a single HBT apparatus with two detectors (D_1, D_2) which interrogate two emitters (E_1, E_2), with unequal brightness and different positions within the point-spread function. The same PSF, indicated by the 2D Gaussian, is monitored by two single-photon detectors that are monitored in coincidence. The solid circle depicts the standard deviation of the Gaussian PSF. (b) HBT output for (a): Second-order correlation function (normally shown as a function of τ, the delay time between photon arrival times) having relative brightness of $\alpha = 0.3$ and the same spontaneous emission rate Γ as a function of the normalized time lag between photon arrival times, $\tau\Gamma$. Also highlighted is the well-known result of $g^{(2)}(0) = 0.5$ (dot-dashed line) for two equal brightness emitters, and the dotted line shows the result for a single emitter for comparison.

we are most concerned with the coincidences at $\tau = 0$, i.e., $g^{(2)}(0)$.

It is often erroneously claimed that $g^{(2)}(0) < 0.5$ implies that one single-photon emitter is being observed. This claim is due to the well-known result that for n co-located emitters of equal brightness, $g_n^{(2)}(0) = (1 - 1/n)$. However, this result does not hold in the case that the intensities as measured from the emitters are not equal. For two emitters of unequal brightness,

$$g_2^{(2)}(0) = \frac{2P_1P_2}{(P_1 + P_2)^2} = \frac{2\alpha}{(1 + \alpha)^2}, \qquad (1)$$

where we have introduced $\alpha = P_2/P_1$ as the ratio of the probability of detecting a photon from particle 2 (P_2) to the probability of detecting a photon from reference particle 1 (P_1). As the probability of photon detection is directly proportional to the received power from a given emitter, this result demonstrates the role of the HBT measurement in determining brightness asymmetry.

By exploring the partial derivative

$$\frac{\partial g_2^{(2)}(0)}{\partial \alpha} = \frac{2(1-\alpha)}{(1+\alpha)^3}, \tag{2}$$

we observe that $g_2^{(2)}(0)$ is most sensitive to the brightness asymmetry when α is small, although it should be noted that the absolute number of recorded coincidences will also be small in this limit.

The difference in the measured brightness of the emitters can be from any cause, for example, because the two emitters are of different species. Equally, however, the difference in brightness could be due to the two emitters being located at different positions relative to the center of the PSF used to interrogate them, and it is this that provides a method of localization. Figure 2(a) shows the relation between α and $g_2^{(2)}(0)$, which highlights the singular case where $g_2^{(2)}(0)$ achieves its maximum value of 0.5 when $\alpha = 1$.

To move our result from an observation about HBT signals to a mechanism for particle localization, we define $P_{0,i}$ as the maximum probability of detecting a photon from emitter $i = 1, 2$, when that emitter is positioned at the center of the detection PSF. We term $P_{0,i}$ the intrinsic brightness of emitter i. The $P_{0,i}$ are directly proportional to the brightness of the emitters and we assume that the overall measurement efficiency of the microscope is the same for each particle. For simplicity, we treat the microscope PSF as a Gaussian, which is good for two dimensions [34]. Although such a treatment is not ideal for practical microscopy [35], it serves to illustrate our method and the use of more complicated PSFs will not alter our results significantly. More generally, our methodology could be used for any PSF, for example, structured illumination [13], although we do not consider such cases here.

Considering the effects of a Gaussian PSF, the probability of detecting a photon from emitter i is

$$P_i = P_{0,i} \exp\left[-r_i^2/(2\sigma^2)\right], \tag{3}$$

where r_i is the in-plane distance from the emitter to the origin of the detection PSF and $\sigma \approx 0.21\lambda/NA$ is the standard deviation of the effective Gaussian PSF for wavelength λ and numerical aperture NA. By comparing $g_2^{(2)}(0)$ with the total intensity which is proportional to the sum of probabilities of detecting photons at a given time, $I \propto P_1 + P_2$, we observe that the two techniques provide qualitatively different information. Figure 2(b) shows $I/(P_{0,1} + P_{0,2})$ with $g_2^{(2)}(0)$ as functions of r_1 and r_2 for the case $\alpha = 1$. A given measurement of both $I/(P_{0,1} + P_{0,2})$ and $g_2^{(2)}(0)$ therefore determines both r_1 and r_2 up to ambiguity in the labeling. The case is only slightly more complicated for $\alpha \neq 1$ [Fig. 2(c), which shows the corresponding contours for $\alpha = 0.5$], where the symmetry between r_1 and r_2 is broken.

Before we discuss the significance of our results for imaging protocols, we first discuss the results expected for HBT experiments under different conditions.

The first case to consider is when the number of particles is not exactly two. This is important as in practical imaging cases, the number of emitters will not be known *a priori* and must be determined during the course of experimentation. Here the use of HBT, and especially higher-order correlations,
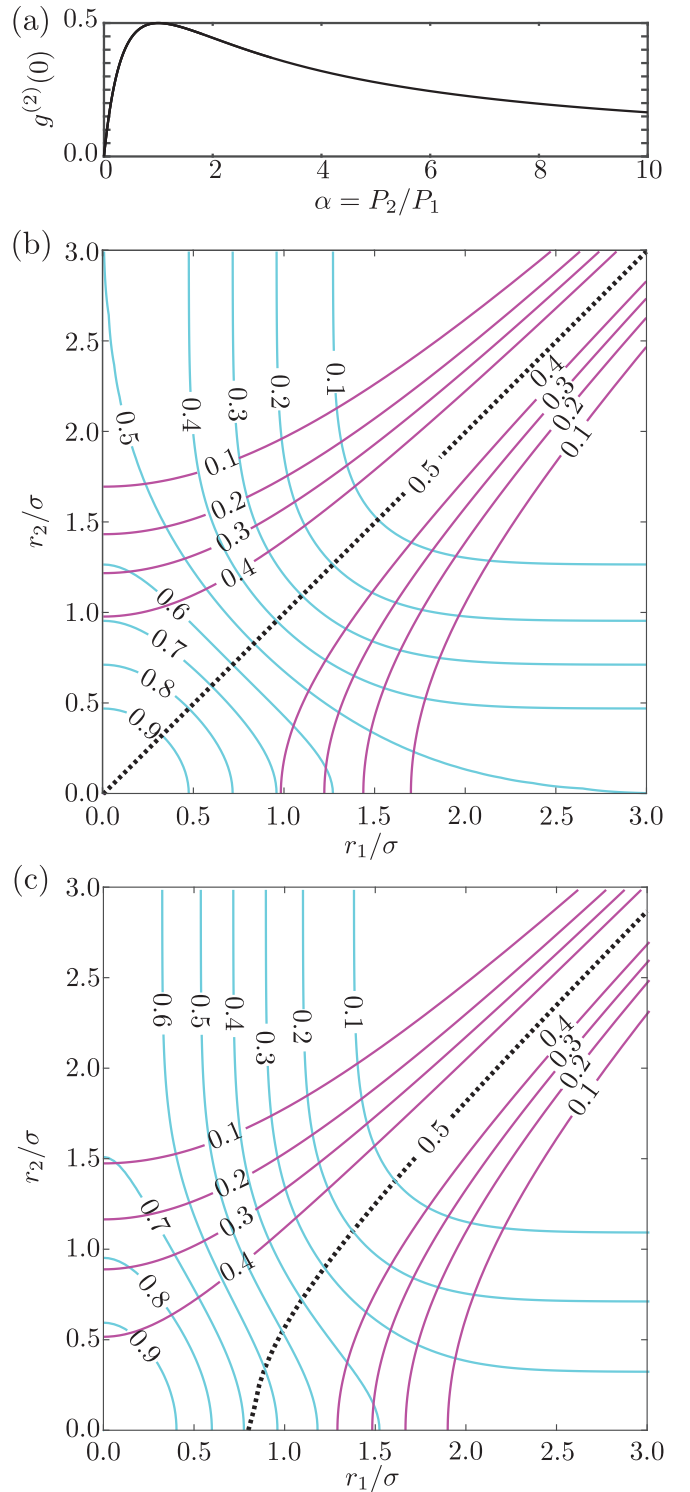

FIG. 2. (a) Cross-correlation function $g^{(2)}(0)$ for two particles as a function of relative brightness, α. The maximum value of $g^{(2)}(0) = 0.5$ is achieved for equal brightness particles. (b) Overlapped contour plots of $I(r_1, r_2, \alpha)$ [magenta (gray)] and $g^{(2)}(\tau = 0, r_1, r_2, \alpha)$ [cyan (light gray)] for $\alpha = 1$, and (c) $\alpha = 0.5$ where radial distance is measured in units of the standard deviation of the PSF of the illumination and collection optics. By comparing both I and $g^{(2)}$, more information about the particles' positions is obtained than is possible using intensity alone. When $\alpha \neq 1$, the symmetry between the contours for r_1 and r_2 is broken and can be seen in the line of constant $g^{(2)}$ (black dashed line).

can be beneficial, as trivially $g_n^{(m)}(0) = 0$ when $m > n$. However, in practice, the time taken to experimentally determine that a high-order correlation is zero, especially in the presence of noise, can be prohibitive, e.g., due to dark counts. For that reason, we will restrict our subsequent localization protocols to the case of second-order correlations only, although we present some of the more general results here for completeness.

We assume N single-photon emitters, labeled without loss of generality from highest intrinsic brightness, 1, to lowest, N. The second-order correlation function is given by the sum of the possible ways that we can observe detector clicks at $\tau = 0$, divided by the possible ways to observe uncorrelated detector clicks (i.e., $\tau = \pm\infty$),

$$g_N^{(2)} = \frac{2 \sum_{i=1}^{N-1} \sum_{j=i+1}^{N} P_i P_j}{\sum_{i=1}^{N} \sum_{j=1}^{N} P_i P_j}. \qquad (4)$$

We explore Eq. (4) for two important cases: three particles in the field of view and two particles against some background.

For the case of three emitters, Eq. (4) reduces to

$$g_3^{(2)} = \frac{2(P_1 P_2 + P_1 P_3 + P_2 P_3)}{(P_1 + P_2 + P_3)^2} = \frac{2(\alpha + \beta + \alpha\beta)}{(1 + \alpha + \beta)^2}, \qquad (5)$$

where we have introduced $\alpha = P_2/P_1$ and $\beta = P_3/P_1$.

Considering the case of a background of weak single-photon emitters, we assume $\mathcal{N}$ background emitters, each with relative emission probability $\gamma = P_{\text{bg}}/P_1$ where $\gamma \ll 1$,

but $\mathcal{N}\gamma \lesssim \alpha$ and is therefore non-negligible,

$$g_{\text{bg}}^{(2)}(0) = \frac{2\left[\alpha + (1+\alpha)\mathcal{N}\gamma + \frac{(\mathcal{N}\gamma)^2}{2}\right]}{(1+\alpha)^2 + (1+\alpha)\mathcal{N}\gamma + (\mathcal{N}\gamma)^2}. \qquad (6)$$

Dark counts can be accounted for using the same treatment assuming that the dark-count rate on each detector is equal.

Lastly, although our subsequent results do not use the full time dependence of the HBT signal, we present them here for completeness. Additionally, any practical experimental system will have a finite resolution, so that the number of counts registered in the $\tau = 0$ bin will in fact be from some finite range $0 < \tau < \delta$. We assume that we are pumping the single-photon emitters well below saturation. In this limit, conditional on the emitter having emitted at $\tau = 0$, the probability of detecting a second photon at time delay τ is

$$P_i'(\tau) = P_i(\tau = 0)[1 - \exp(-\Gamma_i|\tau|)], \qquad (7)$$

where $P_i(\tau = 0)$ is the same probability of detection used above, Γ_i is the spontaneous-emission rate of emitter i, and the dash is used to denote the fact that this probability is conditional on emission at $\tau = 0$. In the case that $\tau < 0$, the first photon is detected before the second at $\tau = 0$; however, the conditional rates are the same as for $\tau > 0$. In general, one would not decouple the detection probability and spontaneous-emission rate as we have done here; however, it is very convenient to treat these as independent parameters as the probability of photon detection given photon emission is often very small in confocal systems. Under these conditions, the HBT result as a function of τ is given by

$$g_2^{(2)}(\tau) = \frac{P_1(0)P_1'(\tau) + P_1(0)P_2(\tau) + P_2(0)P_1(\tau) + P_2(0)P_2'(\tau)}{P_1(0)P_1(\infty) + P_1(0)P_2(\infty) + P_2(0)P_1(\infty) + P_2(0)P_2(\infty)}. \qquad (8)$$

Because we are assuming that the two emitters are well below saturation, $P_i(0) = P_i(\tau) = P_i > P_i'(\tau)$, Eq. (8) reduces to

$$g_2^{(2)}(\tau) = \frac{2P_1 P_2 + P_1^2[1 - \exp(-\Gamma_1|\tau|)] + P_2^2[1 - \exp(-\Gamma_2|\tau|)]}{(P_1 + P_2)^2}. \qquad (9)$$

This result was shown in Fig. 1(b) for the case $\alpha = 0.3$ and $\Gamma_1 = \Gamma_2$.

By considering finite bin width, we may integrate the number of expected coincidences around $\tau = 0$ over a time bin from 0 to δ relative to the number of coincidences in a bin for large τ to obtain the modified result expected for g_2^2 due to finite binning, which we write as

$$\mathfrak{g}_2^{(2)}(\delta) = 1 + \frac{(e^{-\delta\Gamma_1} - 1)P_1^2}{\delta\Gamma_1(P_1 + P_2)^2} + \frac{(e^{-\delta\Gamma_2} - 1)P_2^2}{\delta\Gamma_2(P_1 + P_2)^2} \qquad (10)$$

$$= \frac{2P_1 P_2}{(P_1 + P_2)^2} + \frac{(\Gamma_1 P_1^2 + \Gamma_2 P_2^2)\delta}{2(P_1 + P_2)^2} + O[\delta^2]. \qquad (11)$$

These analytical results show some of the experimental details that are practically necessary for implementing trilateration. However, in what follows, we assume no background, no finite time bin, and only two emitters in the field of view for clarity.

III. MINIMUM MEASUREMENT LOCATIONS: HBT TRILATERATION

On the basis of three measurement locations and six measurement outcomes [three intensity and three $g_2^{(2)}(0)$] taken at the detector locations, our approach computes the least-square error between predicted values of the measured quantities and trial locations for two emitters. We stress that the intensity result can be obtained simply from the square root of the number of coincidences obtained at $\tau = \pm\infty$, and so does not require an additional detector or detector channel. Alternatively, all of the required data could be obtained from a photon-resolving detector at each measurement location where $g_2^{(2)}(0)$ is given by the number of two-photon measurements per unit time divided by the square of the number of single-photon measurements per unit time, with only minor changes to the equations above. Nevertheless, the standard HBT two-detector setup is the most common experimental apparatus for performing such measurements, so that is our focus here.

Without optimizing the detector locations, we note the following heuristics for their placement relative to the emitters. For our scheme to be beneficial compared to standard methods, we require the emitters to be close with respect to the diffraction limit, so as to be unresolved by conventional means, and so that we obtain a significant number of coincidence detections. For simplicity, we place the detector locations at the vertices of an equilateral triangle spaced one standard deviation σ apart based on the illumination PSF.

Our simulation stochastically assigns real-space locations to two single-photon emitters inside one standard deviation of the PSF, σ, with all position results scaled in units of σ. Additionally, we randomly choose the relative power of the emitters, $0 \leqslant \alpha \leqslant 1$, without loss of generality (if we have $\alpha > 1$, relabeling the emitters retrieves $\alpha < 1$). As a first treatment of experimental noise, we introduce a relative error in all of our simulated measurements of η. This error rate is a simple proxy for measurement noise, which is expected to scale as $1/\sqrt{N}$, where N is the number of detected coincidences for $g^{(2)}(0)$. For simplicity, we also use this same value to apply noise to I; this is a considerable overestimation of the intensity noise.

Using the analytical results from Eqs. (1) and (3), our code adds relative errors at the level η, i.e., for each detector position $j = 1, 2, 3$, we generate simulated measurement results,

$$G_j^{(k)} = [1 + \eta \text{RANDN}]g_j^{(k)} \qquad (12)$$

where RANDN is the MATLAB [36] function generating a normally distributed random value with mean 0 and standard deviation 1, $k = 1$ (2) denotes intensity (HBT), and we have dropped the (0) from the $g^{(2)}(0)$ and $G^{(2)}(0)$. Using these synthetic measurement results, we then attempt to determine the emitter positions and relative intensity that minimize the sum of the squared errors, i.e.,

$$\chi^2 = \Sigma_{i,j}\big[\mathcal{G}_j^{(k)}(x_1, y_1, x_2, y_2, \alpha) - G_j^{(k)}\big]^2, \qquad (13)$$

where $\mathcal{G}_j^{(k)}(x_1, y_1, x_2, y_2, \alpha)$ is the expected value of $k = 1$ intensity or $k = 2$ HBT coincidence, for detector location j for the trial values $x_1 \ldots \alpha$.

The results of performing such a trial are shown in Fig. 3 where two emitters were randomly placed at $(x_1, y_1) = (-0.6300, -0.1276)$, $(x_2, y_2) = (0.5146, -0.5573)$, $\alpha = 0.3617$, and $\eta = 0.1$. Figure 3(a) shows the expected results of performing a standard confocal scan (normalized with the maximum powers of the emitters) $I/(P_{0,1} + P_{0,2})$: the two emitters are not resolved. Figure 3(b) shows contours of $g^{(2)}(0)$, such as would be obtained by scanning an HBT setup. The contours of constant $g^{(2)}(0)$ are parallel to each other and we conclude that for two emitters, there is a significant amount of redundant information in the full $g^{(2)}$ map. The optimal measurement strategy for two-particle localization is therefore still unclear when considering more than the minimal number of measurement locations that we demonstrate here.

For quantum trilateration, we consider three detector positions, $(0, 1)$, $(\sqrt{3}/2, -0.5)$, and $(-\sqrt{3}/2, -0.5)$. We then compute 501 trials using the method outlined in Eq. (12) and independently determined the expected emitter locations using the MATLAB routine FMINSEARCH to gauge the error. The
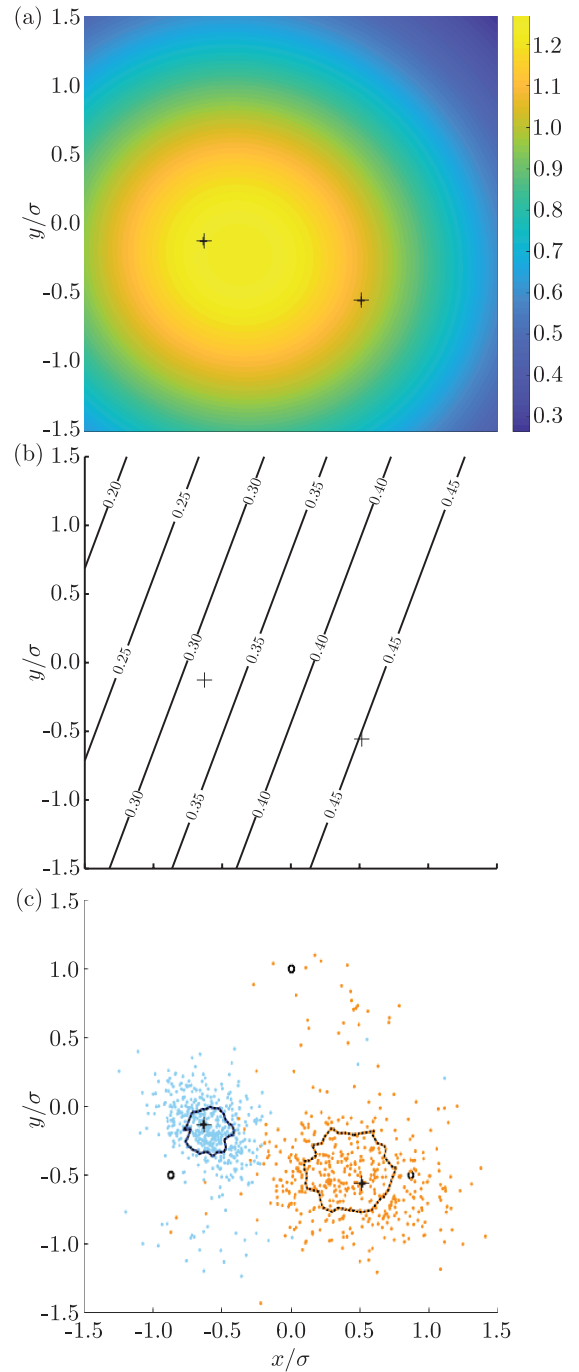

FIG. 3. Imaging of two single-photon emitters at $(x_1, y_1) = (-0.6300, -0.1276)$, $(x_2, y_2) = (0.5146, -0.5573)$, $\alpha = 0.3617$, and $\eta = 0.1$. The emitters are shown by the plus symbols in each subfigure. (a) Pseudo-color plot showing a predicted confocal map for a single detector, scanned over the emitters. The exact location of the emitters is not well resolved. (b) Contours of $g^{(2)}(0)$ for a scanned HBT apparatus. The contours are perpendicular to the line joining the two emitters. Although $g^{(2)}(0)$ provides some information on particle locations, there is significant redundancy. (c) Results of 501 trilateration reconstructions. Black open circles mark the detector locations and the dots are the calculated locations of emitters 1 and 2, respectively, for each numerical experiment where the confidence intervals represent 39.5% of closest reconstructions. The effective PSFs are shown by the irregular polygons. All subfigures have the same x axis.
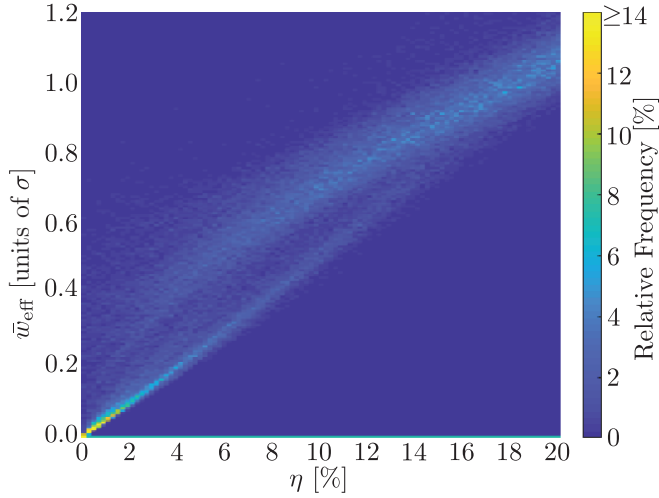
FIG. 4. Histograms showing average PSF width, $\bar{w}_{\text{eff}}$, after applying the trilateration protocol for randomly chosen emitters for each η. The color of each precision-η point shows the fraction that precision was achieved under those noise conditions. Observe the presence of two bands within the results. The lower band is obtained for $\alpha \lesssim 0.5$, and the upper for cases where $0.5 \lesssim \alpha \leqslant 1$.

results of individual runs are shown by the blue (gray) and orange (light gray) dots for emitter 1 and emitter 2, respectively, which accord well with the true locations. Occasionally, pathological cases can greatly skew the fitting [37].

To provide a fair comparison with conventional microscopy, we define an effective width of the distribution of the reconstructions. To achieve this, we order the inferred particle positions by radial distance to the centroid of the reconstructions. Then we determine the radial distance between the centroid of the inferred positions and the position of the $\lceil (1 - 1/\sqrt{e})N \rceil^{\text{th}}$ reconstruction, $\rho_{39.5\%}$. If this distribution were perfectly Gaussian, then $\rho_{39.5\%}$ would correspond to the standard deviation of the PSF, with $2\rho_{39.5\%}$ being the width of the PSF. In our case, it is not a given that the distribution of the reconstructions will be Gaussian. Accordingly, we instead determine the area that includes the closest 39.5% of the reconstructions, which we write as $A_{39.5\%}$. We then define the effective width of the trilateration reconstruction as

$$w_{\text{eff}} \equiv 2\sqrt{\frac{A_{39.5\%}}{\pi}}. \qquad (14)$$

As we obtain an effective width for each emitter, we take the average of the widths, $\bar{w}_{\text{eff}} = (w_{\text{eff},1} + w_{\text{eff},2})/2$, to determine the effectiveness of the protocol. This width can then be used to determine the super-resolution improvement factor where that exists, by comparing with the original confocal PSF width $w_{\text{cf}} = 2\sigma$. In the case provided in Fig. 3(c), we find the widths of the effective PSFs, $w_{\text{eff},1} = 0.3724$ and $w_{\text{eff},2} = 0.6415$. The average width of the effective PSF in this case is $\bar{w}_{\text{eff}} = 0.5069$, which corresponds to a modest improvement over the diffraction limit for a Gaussian PSF of 1.97 times.

To quantify the scaling of our protocol's precision with detection noise, we show a series of histograms (Fig. 4) of $\bar{w}_{\text{eff}}$ for an ensemble of 720 randomly chosen emitter locations and relative brightnesses $(x_1, y_1, x_2, y_2, \alpha)$, trialed

501 times apiece per value of system noise $0 \leqslant \eta \leqslant 0.20$. When $\alpha \lesssim 0.05$, our protocol fails to locate the less bright emitter, although the brighter emitter is localized. Note that for small η, the relative frequency in some of the histogram bins exceeds 14% and the maximum bin occupancy is 60%.

Clearly noticeable are two distinct bands of data. The lower of the two bands corresponds to the case where $\alpha \gtrsim 0.5$, which demonstrates a linear scaling of localization with η or, equivalently, with $1/\sqrt{N}$, as the main uncertainty is counting statistics. The upper band, attained for $0.5 \lesssim \alpha < 1$, is more interesting. We see that for comparable η, the localization error is greater. This indicates that when there is a large difference in the intrinsic brightness of the emitters, the protocol shows better scaling than when the two emitters are of comparable brightness. This result is in keeping with the analysis around the rate of change from Eq. (2).

The above method for incorporating errors is simple to understand and provides an approximation to a proper treatment of noise from sources including (especially in our context) the counting statistics due to a finite number of events. However, it does not fully capture the physics of the situation, including the differences in the number of events expected for bright and dim particles, and the different number of events detected at each detector as a function of the relative positions of the emitters within the PSF. Accordingly, we have recalculated the data by setting a detection time interval t, and for each random instance determined the received numbers of counts for emitter i, c_i, and coincidences c_{12} received at each detector,

$$c_1 = \text{POISSRND}(P_1 t), \qquad (15)$$

$$c_2 = \text{POISSRND}(P_2 t), \qquad (16)$$
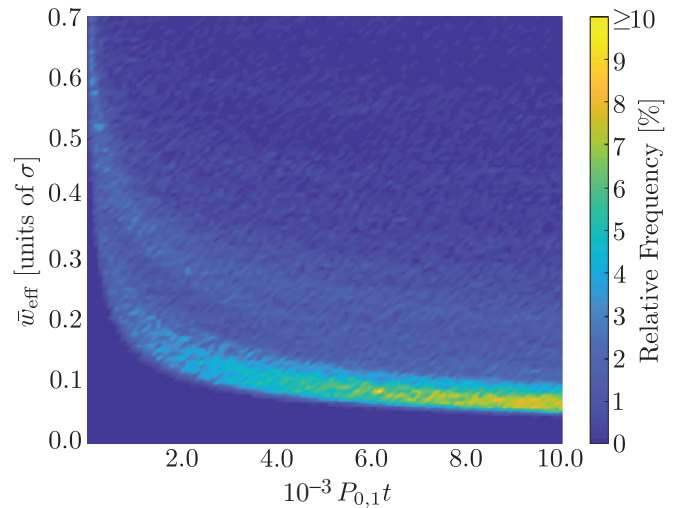
$$c_{12} = \text{POISSRND}(P_1 P_2 t^2), \qquad (17)$$

FIG. 5. Histograms showing average PSF width, $\bar{w}_{\text{eff}}$, after applying the trilateration protocol for randomly chosen emitters for increasing detection time. As with Fig. 4, the color of each pixel shows the relative occurrence of that localization precision within the total number of (randomly) selected configurations. The two bands with α are still visible here, with $\alpha \lesssim 0.5$ yielding significantly better localization than $\alpha > 0.5$. Note that the $P_{0,1}t$ axis starts at 10, not 0.
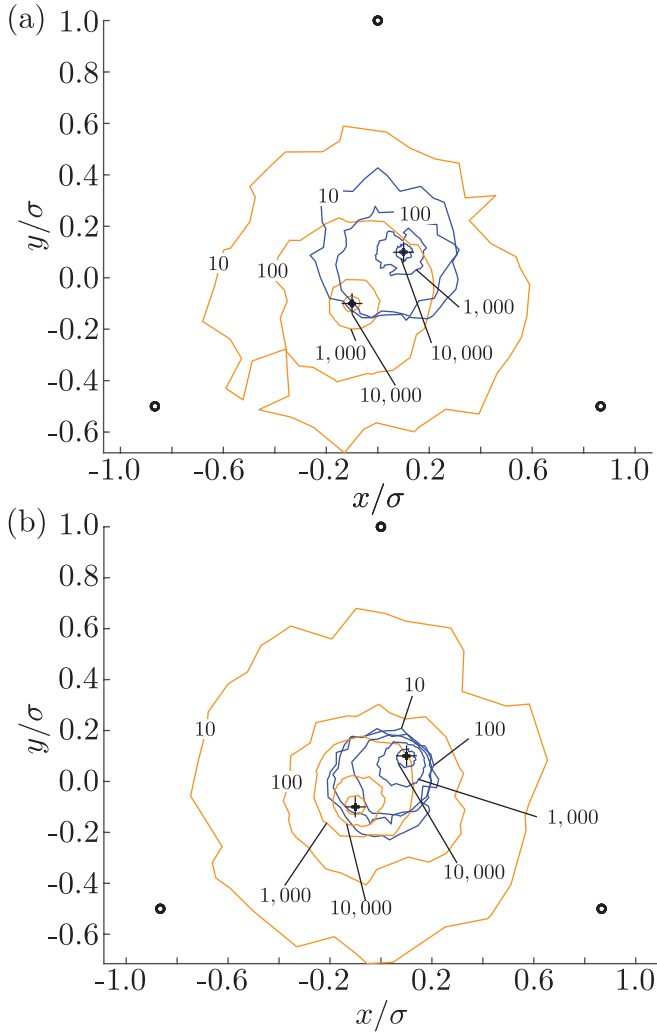
FIG. 6. Localization as a function of measurement time in units of inverse photon arrival rate. The two cases show the expected uncertainties for 501 reconstructions for times of $P_{0,1}t = 10, 100,$ 1000, 10 000 and 100 000 at each detector location. Particle locations were $(x_1, y_1) = (-0.1, -0, 1)$ and $(x_2, y_2) = (0.1, 0.1)$ with (a) $\alpha = 0.3617$ and (b) $\alpha = 0.8000$. As before, the detector locations are shown by open circles, and the ground truth particle locations are indicated with plus signs. The orange (light gray) contours show the effective point-spread function for particle 1, and the blue (dark gray) contours show the effective point-spread function for particle 2. The contours are labeled by the appropriate $P_{0,1}t$ product, except for the innermost $P_{0,1}t = 100\,000$. Full results are shown in Table I. Note that the contours do not always easily resolve, especially in the case of (b), which is a consequence of the stochastic nature of the noise used in the protocol.

where POISSRND is the MATLAB [36] function to generate a Poisson-distributed random variable. These counts are then used to generate the $G_j^{(2)} = 2c_{12}/(c_1 + c_2)^2$ at each detector location, and the fitting proceeds as before.

The result of performing such counting-based reconstructions is shown in Fig. 5 as a function of acquisition time, where $t = 1/P_{0,1}$ corresponds to the mean time for a photon to be detected from particle 1 if it were located in the maximum

of a PSF. As before, the two bands for different α are visible. The overall scaling with t will be discussed in the next section.

To illustrate the scaling of the effective width with increased measurement time, Fig. 6 shows two cases for close emitters located at $(x_1, y_1) = (-0.1, -0, 1)$ and $(x_2, y_2) = (0.1, 0.1)$, for $\alpha = 0.3617$ [Fig. 6(a)] and $\alpha = 0.8000$ [Fig. 6(b)]. The trilateration results for these configurations are presented in Table I. As the case in Fig. 6(a) has $\alpha \lesssim 0.5$, we observe significantly better convergence of the protocol than the case in Fig. 6(b), in keeping with the intuition developed from Eq. (2) and Figs. 4 and 5.

IV. EFFECTS OF INCREASING THE NUMBER OF MEASUREMENT LOCATIONS: MULTILATERATION

Although the trilateration case is interesting for exploring a minimal condition necessary for demonstrating quantum superiority over classical localization for two particles, it is not obvious that it is, in any way, optimal. As such, here we illustrate the effect of increasing the number of measurement locations, considering four, five, and six locations. Because there are many possible configurations and possibly an (unknown) optimal set of measurement locations, for simplicity we restrict ourselves to a case that affords easy comparison between the different configurations. We therefore set the measurement locations to be equally spaced around the circumference of a circle of diameter 2σ. The locations are depicted schematically in Fig. 7.

As with the case of trilateration, we perform a series of numerical experiments, 640 randomly chosen configurations of position and relative intrinsic brightness, for increasing measurement time. The resulting histograms for four, five, and six locations are presented in Fig. 8, which shows qualitatively similar improvements in localization with increasing the number of measurement locations.

To quantify the scalings, in Fig. 9 we show the $\bar{w}_{\rm eff}$ of the mode of the histograms, i.e., the most likely scaling of the average effective PSF averaged over all configurations. We also provide a comparison with a comparable intensity-only localization method (discussed below). This scaling gives an effective heuristic to predict the scaling for "reasonable" configurations (noting that certain cases have worse scaling than this). We fit this scaling with a straight line on a log-log plot. This gave scaling laws of the form

$$\bar{w}_{{\rm eff},j} = 10^{a_j} t^{b_j}, \tag{18}$$

where a_j and b_j were determined by the fits, and j denotes the number of detector locations.

The values empirically determined from the fits for lateration in Fig. 9 are

$a_{03} = 0.7893,$	$b_{03} = -0.4952,$
$a_{04} = 0.7402,$	$b_{04} = -0.5023,$
$a_{08} = 0.5592,$	$b_{08} = -0.4908,$
$a_{09} = 0.5551,$	$b_{09} = -0.4981,$
$a_{11} = 0.5203,$	$b_{11} = -0.5005,$
$a_{12} = 0.5202,$	$b_{12} = -0.5044,$
$a_{24} = 0.3586,$	$b_{24} = -0.5009.$

TABLE I. The ground truth and algorithmically determined parameters for the cases shown in Fig. 6. As expected, the case for $\alpha \lessgtr 0.5$ shows greater precision (enhanced localization) compared with the case $0.5 \lessgtr \alpha$. SF is the predicted super-resolution factor.

Time	(x_1, y_1)	(x_2, y_2)	α	$w_{\text{eff},1}$	$w_{\text{eff},1}$	$\bar{w}_{\text{eff}}$	SF
Ground truth (a)	$(-0.1, -0.1)$	$(0.1, 0.1)$	0.3617				
10	$(0.4638, -0.1234)$	$(-0.6781, 0.0614)$	0.3565	1.1603	0.5382	0.8493	1.1774
100	$(-0.3435, -0.5961)$	$(0.2430, 0.3595)$	0.4158	0.6186	0.4437	0.5311	1.8829
1000	$(0.0313, -0.1288)$	$(-0.0316, 0.1167)$	0.3658	0.1943	0.1732	0.1838	5.4407
10 000	$(-0.1396, -0.1000)$	$(0.1377, 0.1087)$	0.3622	0.0618	0.0601	0.0609	16.4204
100 000	$(-0.1255, -0.1066)$	$(0.1247, 0.1046)$	0.3617	0.0196	0.0207	0.0201	49.7512
Ground truth (b)	$(-0.1, -0.1)$	$(0.1, 0.1)$	0.8000				
10	$(-0.1972, 0.7567)$	$(0.1097, -0.1028)$	0.5309	1.3265	0.4110	0.8688	1.1510
100	$(-0.1369, 0.0408)$	$(0.0671, -0.0095)$	0.6663	0.6785	0.3698	0.5241	1.9080
1000	$(0.2648, 0.3235)$	$(-0.2664, -0.3145)$	0.7706	0.3999	0.3079	0.3539	2.8257
10 000	$(-0.1579, 0.0719)$	$(0.1470, -0.0735)$	0.8079	0.1980	0.1764	0.1872	5.3419
100 000	$(-0.0853, -0.0729)$	$(0.0860, 0.0728)$	0.8010	0.0758	0.0703	0.0730	13.6986

These values show approximately $1/\sqrt{t}$ scaling for the precision, independent of the number of detector locations as expected, and it is likely that increasing the number of histograms will yield scaling closer to $b = -0.5$.

Figure 9 shows scaling comparisons between intensity only (upper band of data) and lateration (lower band of data). For consistency between the methods, both use the detector geometry as shown in Fig. 7. For intensity-only localization, the trends show worse than $1/\sqrt{t}$ scaling. This shows that for the same number of detectors in the same collection time, lateration provides greater localization of emitters. One reason for the poor scaling of the intensity-only localization in our configuration is that intensity-only localization requires many measurement locations and benefits from a rectangular grid. Nevertheless, our results show that quantum lateration is supe-

rior to intensity-only for comparable measurement locations. We find that the intensity-only protocol fails to localize the
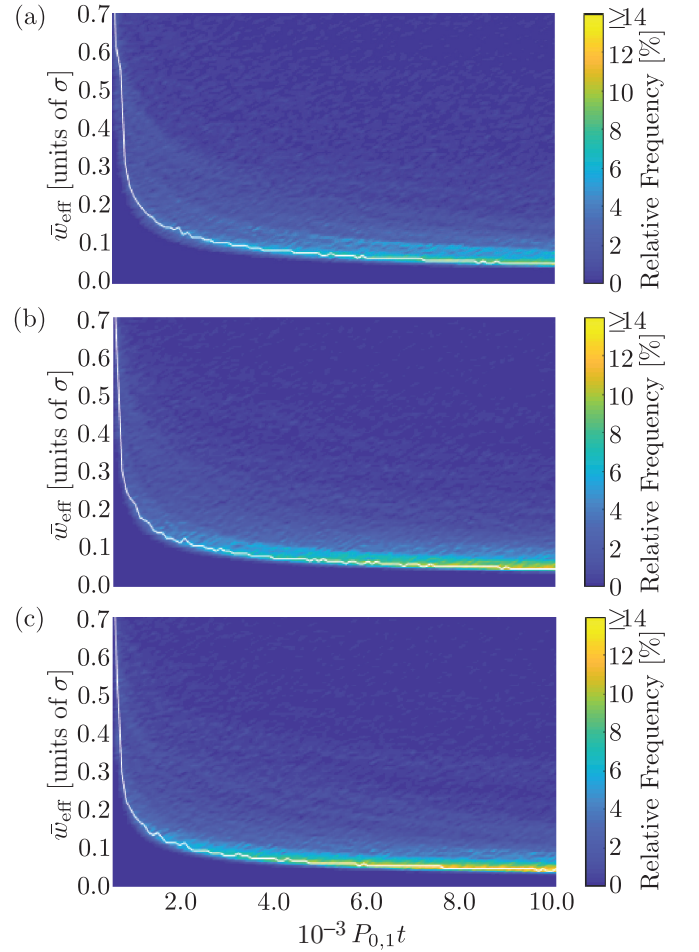
FIG. 8. Histograms showing effective PSF width, $\bar{w}_{\text{eff}}$, for randomly chosen emitters as a function of total measurement time for (a) four, (b) five, and (c) six measurement locations. The modal scaling has been highlighted with the white line. In all cases, we observe qualitatively similar improvements in effective PSF with increasing measurement time. Note that the $P_{0,1}t$ axis starts at 10, not 0.
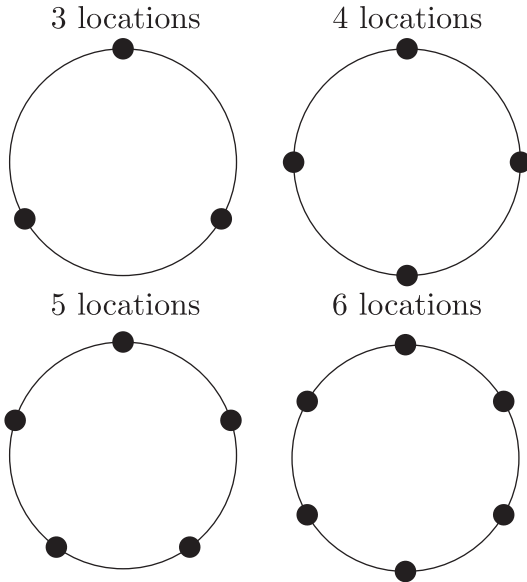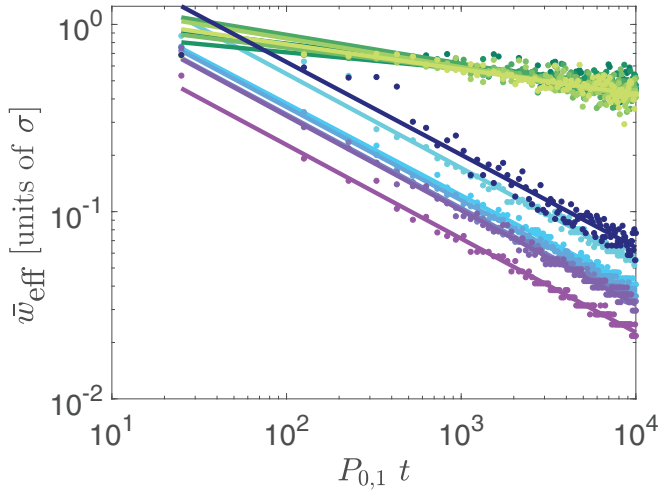

FIG. 7. Schematic of the relative positions of the detector locations used to explore the scaling with increasing number of detector locations. The detectors were equally spaced around the circumference of a circle of diameter 2σ, corresponding to the original width of the point-spread function.

FIG. 9. Scaling of the mode of the histogram of $\bar{w}_{\text{eff}}$ as a function of total measurement time, which is a measure for the expected location's scaling. The green (upper) band depicts classical intensity-only precision localization scaling with 7, 8, 9, 10, 11, and 12 detectors. The blue or purple (lower) band depicts scaling for our quantum lateration model for 3, 4, 8, 9, 11, 12, and 24 measurement locations. The histogram mode data are shown by dots, whereas the solid lines are the fits. For the multilateration cases, each histogram mode is the result from 10 000 random measurement locations. We observe an improvement with more detector locations, as well as consistent, approximately $1/\sqrt{t}$ scaling in the localization precision, independent of the number of locations.

second emitter with high precision, which reduces the overall average effective point-spread function. We can see that with comparable measurement locations, lateration provides greater emitter localization than intensity localization.

To clarify this point, consider the time required to achieve the same precision (on average) with three and four detector locations (assuming that the $b_i = -1/2$). This implies that

$$\frac{t_3}{t_4} = \left(\frac{10^{a_3}}{10^{a_4}}\right)^2. \tag{19}$$

However, measuring at four detector locations either uses one HBT system for 4/3 times longer or uses an additional HBT setup in parallel. If we just take the case of a single HBT system that is moved between the (predetermined) locations, by comparing the results for $j < k$ detector locations, we should conclude that it is preferable to use more detector locations if

$$\left(\frac{10^{a_j}}{10^{a_k}}\right)^2 > \frac{k}{j}. \tag{20}$$

We explore this inequality by calculating $\left(\frac{10^{a_j}}{10^{a_k}}\right)^2 - \frac{k}{j}$ for multilateration:

a_j/a_k	4	8	9	11	12	24
3	−0.2615	−1.0442	−1.1488	−1.3765	−1.4617	−2.4574
4		−0.7550	−0.8470	−1.0556	−1.1294	−2.0341
8			−0.0700	−0.2582	−0.3105	−1.1019
9				−0.1825	−0.2318	−0.9969
11					−0.0447	−0.7879
12						−0.7249

The multilateration inequalities imply that in this test, more measurements equate to better localization. However, as mentioned, our heuristic approach does not guarantee optimal (information-theoretic and adaptable) placement of those locations, and thus a fair comparison is not necessarily achieved. Further work is required to establish the optimal detector locations for a given system.

V. CONCLUSIONS

Our results present a minimal demonstration of the advantage achieved using QCM. We have shown that by combining quantum correlation with conventional intensity measurements, it is possible to solve the quantum multilateration problem for two particles of unknown relative intensity: a problem impossible to solve on the basis of intensity measurements alone. This methodology highlights the additional information accessible to Hanbury Brown and Twiss measurements that is not present in conventional confocal-type measurements, thereby clarifying the origin of the speedup seen in quantum microscopy [1–3,11,12,38–40].

Although all three measurement locations are necessary for the localization of the two particles, it is important to stress that in general, the HBT signal provides little nonredundant information. For example, the HBT signal is trivially zero at every point where there is no received intensity, and even when the intensity is nonzero, there are many points where the HBT result gives the same value. Indeed, for two particles that are exactly, or almost, co-located, there is little variation in the HBT value over the scene (see contours in Fig. 2). Nevertheless, the three unique measurement locations are still necessary for the two-particle trilateration protocol. This leaves open the issue of the optimal light budget to localize the particles with the least total number of measurements.

By showing that only three measurement locations are required for super-resolution localization of two particles, our results are significant in the search for optimal strategies for microscopy. Optimal microscopy is necessary, as effects such as phototoxicity limit the application of super-resolution methods in biology, and it is therefore necessary to quantify the total photon budget necessary to obtain a desired resolution in any experiment. Our results are normalized in units of the excitation field PSF. However, although we have compared our results with standard confocal microscopy, there is no restriction on the microscopy technique. So quantum multilateration could be combined with other super-resolution techniques, for example, stimulated emission depletion (STED)

microscopy, and our approach would provide commensurate increases to the obtained STED resolution, as shown above.

We also show that increasing the number of detector locations provides improved resolution, and that this improvement is better than would be expected simply on the basis of taking more measurements at fewer locations. We also note that this process may be further optimized through information-theoretic and adaptive techniques, e.g., deep learning and artificial intelligence, which have been demonstrated in super-resolution single-molecule microscopy [41].

[1] S. W. Hell and J. Wichmann, Opt. Lett. **19**, 780 (1994).

[2] M. J. Rust, M. Bates, and X. Zhuang, Nat. Methods **3**, 793 (2006).

[3] M. Sauer, J. Cell Sci. **126**, 3505 (2013).

[4] P. Hemmer and J. S. Ben-Benjamin, Phys. Scr. **91**, 093003 (2016).

[5] P. R. Hemmer and T. Zapata, J. Opt. **14**, 083002 (2012).

[6] V. Giovannetti, S. Lloyd, and L. Maccone, Science **306**, 1330 (2004).

[7] V. Giovannetti, S. Lloyd, and L. Maccone, Nat. Photon. **5**, 222 (2011).

[8] R. Hanbury Brown and R. Q. Twiss, Nature (London) **177**, 27 (1956).

[9] O. Schwartz and D. Oron, Phys. Rev. A **85**, 033812 (2012).

[10] S. W. Hell, J. Soukka, and P. E. Hänninen, Bioimaging **3**, 64 (1995).

[11] O. Schwartz, J. M. Levitt, R. Tenne, S. Itzhakov, Z. Deutsch, and D. Oron, Nano Lett. **13**, 5832 (2013).

[12] D. Gatto Monticone, K. Katamadze, P. Traina, E. Moreva, J. Forneris, I. Ruo-Berchera, P. Olivero, I. P. Degiovanni, G. Brida, and M. Genovese, Phys. Rev. Lett. **113**, 143602 (2014).

[13] A. Classen, J. von Zanthier, M. O. Scully, and G. S. Agarwal, Optica **4**, 580 (2017).

[14] M. K. Cheezum, W. F. Walker, and W. H. Guilford, Biophys. J. **81**, 2378 (2001).

[15] A. J. T. S. Mello and D. R. Pipa, Appl. Opt. **55**, 3701 (2016).

[16] Y. Ogi, H. Kohguchi, D. Niu, K. Ohshimo, and T. Suzuki, J. Phys. Chem. A **113**, 14536 (2009).

[17] S. Oppel, T. Büttner, P. Kok, and J. von Zanthier, Phys. Rev. Lett. **109**, 233603 (2012).

[18] M. E. Pearce, T. Mehringer, J. von Zanthier, and P. Kok, Phys. Rev. A **92**, 043831 (2015).

[19] M. Tsang, R. Nair, and X.-M. Lu, Phys. Rev. X **6**, 031033 (2016).

[20] A. Classen, F. Waldmann, S. Giebel, R. Schneider, D. Bhatti, T. Mehringer, and J. von Zanthier, Phys. Rev. Lett. **117**, 253601 (2016).

[21] L. A. Howard, G. G. Gillett, M. E. Pearce, R. A. Abrahao, T. J. Weinhold, P. Kok, and A. G. White, Phys. Rev. Lett. **123**, 143604 (2019).

[22] Y. Altmann, S. McLaughlin, M. J. Padgett, V. K. Goyal, A. O. Hero, and D. Faccio, Science **361**, eaat2298 (2018).

[23] M. B. Kjærgaard, H. Blunck, T. Godsk, T. Toftkjær, D. L. Christensen, and K. Grønbæk, *Pervasive Computing. Pervasive 2010*, edited by P. Floréen, A. Krger, M. Spasojevic, Lecture Notes in Computer Science, Vol. 6030 (Springer, Berlin, Heidelberg, 2010), pp. 38–56.

[24] J. Yeo, P. Lingras, W.-Z. Wu, M. Szczuka, N. Cercone, and D. Slezak, *Rough Sets and Knowledge Technology, RSKT 2007 Proceedings*, Vol. 4481 (Springer, Berlin, 2007), pp. 331–338.

[25] R. H. Webb, Rep. Prog. Phys. **59**, 427 (1996).

[26] G. M. P. Van Kempen, L. J. Van Vliet, P. J. Verveer, and H. T. M. Van Der Voort, J. Microsc. **185**, 354 (1997).

[27] J. Jonkman and C. M. Brown, J. Biomol. Tech. **26**, 54 (2015).

[28] J. Hightower and G. Borriello, Computer **34**, 57 (2001).

[29] D. W. Drumm and A. D. Greentree, Sci. Rep. **7**, 14652 (2017).

[30] M. Bodnar, U. Foryś, and J. Poleszczuk, J. Math. Anal. Appl. **376**, 74 (2011).

[31] S. E. Webb, M. Hirsch, S. R. Needham, B. C. Coles, K. M. Scherer, S. K. Roberts, L. C. Zanetti-Dominingues, C. J. Tynan, M. L. Martin-Fernandez, and D. J. Rolfe, Methods **88**, 76 (2015).

[32] L. C. Zanetti-Dominingues, M. Hirsch, C. J. Tynan, D. J. Rolfe, T. V. Boyadzhiev, K. M. Scherer, D. T. Clarke, M. L. Martin-Fernandez, and S. R. Needham, Prog. Biophys. Mol. Biol. **118**, 139 (2015).

[33] R. M. Donlan and J. W. Costerton, Clin. Microbiol. Rev. **15**, 167 (2002).

[34] B. Zhang, J. Zerubia, and J.-C. Olivo-Marin, Appl. Opt. **46**, 1819 (2007).

[35] S. Stallinga and B. Rieger, Opt. Express **18**, 24461 (2010).

[36] Computer code MATLAB and Statistics Toolbox Release 2018b (MathWorks, Natick, 2018).

[37] N. Hlupić, I. Beroš, and D. Basch, J. Comput. Inf. Technol. **21**, 125 (2013).

[38] A. Muthukrishnan, M. O. Scully, and M. S. Zubairy, J. Opt. B: Quantum Semiclass. Opt. **6**, S575 (2004).

[39] Y. Israel, R. Tenne, D. Oron, and Y. Silberberg, Nat. Commun. **8**, 14786 (2017).

[40] R. Tenne, U. Rossman, B. Rephael, Y. Israel, A. Krupinski-Ptaszek, R. Lapkiewicz, Y. Silberberg, and D. Oron, Nat. Photon. **13**, 116 (2019).

[41] E. Nehme, L. E. Weiss, T. Michaeli, and Y. Shechtman, Optica **5**, 458 (2018).